Scale-by-scale kinetic energy budget near the turbulent/nonturbulent interface

T. Watanabe,[1,*] C. B. da Silva,[2,1] and K. Nagata[1]
[1]*Department of Aerospace Engineering, Nagoya University, Nagoya, Japan*
[2]*LAETA, IDMEC, Instituto Superior Técnico, Universidade de Lisboa, Lisboa, Portugal*

(Received 3 May 2020; accepted 1 December 2020; published 29 December 2020)

A scale-by-scale kinetic energy budget is analyzed near the turbulent/nonturbulent interfacial (TNTI) layer with direct numerical simulations (DNSs) of a local turbulent front evolving without mean shear (shear-free turbulence). A local volume average is used to decompose the flow variables into their large-scale and small-scale components near the TNTI layer. The kinetic energy and interscale energy flux from large to small scales of motion are shown to be severely depleted for small scales within the viscous superlayer. The forward interscale energy transfer from large to small scales near the TNTI layer is mostly caused by the velocity gradient in the interface normal direction while the velocity gradient in the tangential direction transfers, on average, the energy from small to large scales. The velocity gradients that cause the forward energy transfer near the TNTI layer are associated with a compressive motion in the interface normal direction and a shearing motion due to the velocity in the tangential direction. The pressure diffusion increases the kinetic energy near the interface except at small scales within the TNTI layer. The averaged pressure diffusion term at the small scales within the TNTI layer has negative values, which are consistent with the presence of small-scale vortices within the TNTI layer. The transports by turbulent diffusion and interaction between large and small scales are negatively correlated even near the TNTI layer, and their effects are locally canceled by each other as also observed in other turbulent flows.

DOI: 10.1103/PhysRevFluids.5.124610

I. INTRODUCTION

Turbulent flow regions in engineering applications and the natural environment are often surrounded by regions of irrotational flow, where the separation occurs across a very thin layer, the so-called turbulent/nonturbulent interfacial (TNTI) layer [1]. This layer plays an important role in the mechanism of turbulent entrainment, in which regions of nonturbulent fluid become part of the turbulent flow region [2]. Understanding the flow dynamics near this TNTI layer is crucial for modeling, predicting, and controlling turbulent entrainment in many engineering flows. For this reason, the TNTI layer has been extensively studied using direct numerical simulations (DNSs) and experiments in free shear flows [2–10] and boundary layers [11–15].

Since turbulent flows are characterized by a wide range of scales of motion, studying the scale dependence of several flow variables has been of great interest in turbulence research. The most direct method of analysis typically involves studying the turbulent motions in the wave number space. The key quantities of interest here are the kinetic energy spectrum and the energy transfer function, which are both related in the Lin equation [16,17]. In contrast, a similar analysis in the physical space is often based on the second-order velocity structure function, which can be seen

*watanabe.tomoaki@c.nagoya-u.jp

as a measure of the cumulative kinetic energy held below a given length scale. In this context, the Karman-Howarth equation is the counterpart of the Lin equation, and inhomogeneous and anisotropic forms of the Karman-Howarth equation [18] have been used for the interscale analysis of turbulent flows [19–21].

Cimarelli *et al.* [22] employed two-dimensional Fourier transforms to assess the TNTI layer characteristics in the wave number space in DNSs of shear-free turbulence, which resulted in statistics that contain contributions both from the turbulent and nonturbulent regions. It is, however, crucial to rigorously separate the turbulent and nonturbulent flow regions in any credible analysis of the turbulence near the interface because of the very different nature of the two flow regions [3]. Unfortunately, when the classical methods developed for studying interscale energy transfers in turbulent flows are employed to analyze the turbulent flow dynamics near the TNTI layer, information from the turbulent flow region is necessarily contaminated by that from the nonturbulent flow region, and, similarly, nonturbulent statistics invariably contain some information from the turbulent flow region. The conditional statistics that have been developed to study the TNTI layer since [3] allow for a clear separation between the two flow regions by calculating the statistics conditioned on the distance from the TNTI layer. However, they do not provide any information regarding the active scales of motion in the two flow regions.

In a recent work [23], we developed a new procedure that allows a clear separation of the flow variables in the physical space as well as in the space of scales. This approach is based on a local volume average combined with the conditional statistics taken on the local interface coordinate, where the volume average acts as a low-pass filter decomposing a variable into their large-scale and small-scale contributions. This method was used to estimate the integral length scale near the TNTI layer [23]. The filtering approach has been used to investigate the local properties of turbulent energy cascade [24–26]. In the present procedure, the turbulent and nonturbulent flow regions use local volume averages containing only turbulent and nonturbulent fluids, respectively, thus enabling the resulting statistics to reveal the detailed scale dependence of any turbulent fluid variables within the TNTI layer. The kinetic-energy transfer near the TNTI has been studied by using one-point statistics both in experiments [27] and DNS [28]. In the present work, we use the scale decomposition based on the volume average to evaluate the scale-by-scale kinetic energy budgets near the TNTI layer.

II. DIRECT NUMERICAL SIMULATION DATABASE OF SHEAR-FREE TURBULENCE

A DNS database of shear-free turbulence [23] is used for studying the scale-by-scale transport of kinetic energy near the TNTI layer. The shear-free turbulence is a localized turbulent front bounded by a nonturbulent flow region, where the turbulent region spreads in one direction with time, while the flow is statistically homogeneous in the other directions (details of the DNS can be found in Ref. [29]). The direction in which the turbulence spreads is denoted by y while the homogeneous directions are denoted by x and z. Velocity components in x, y, and z directions are denoted by u, v, and w, respectively. The DNS code uses classical pseudospectral methods for spatial discretization and the third-order Runge–Kutta method for temporal advancement. The simulation is performed in a periodic box with size $(2\pi)^3$, using N^3 (collocation) points. The TNTI layer is analyzed with three different DNS of the shear-free turbulence summarized in Table I. Here, the statistics are calculated from a single instantaneous data point in each case. Table I shows the statistics obtained on the center plane of the shear-free turbulence ($y = 0$). In all cases, the spatial resolution Δ is small compared with the Kolmogorov scale $\eta = (\nu^3/\langle\varepsilon\rangle)^{1/4}$, where $\varepsilon = 2\nu S_{ij}S_{ij}$ is the kinetic energy dissipation rate, ν is the kinematic viscosity, $S_{ij} = (\partial u_i/\partial x_j + \partial u_j/\partial x_i)/2$ is the rate-of-strain tensor, and the average $\langle\ \rangle$ is taken in the homogeneous x and z directions as a function of y. Table I also shows the ratio of rms velocity fluctuations in the x and z directions, u_{rms}/w_{rms}, where rms values are defined as $f_{rms} = (\langle f^2\rangle - \langle f\rangle^2)^{1/2}$. These two directions are identical in statistics, and the shear-free turbulence in the present DNS has $u_{rms}/w_{rms} \approx 1$. It should be noted that u_{rms}/w_{rms} deviates from 1 significantly if the computational domain is not large enough because the statistical convergence of the present DNS depends on the domain size in the homogeneous directions.

TABLE I. Parameters of the DNS dataset of shear-free turbulence (SFT). Reynolds number $Re_0 = u_{rms}L/\nu$ (u_{rms} is the rms velocity fluctuation in the x direction, L is the integral length scale calculated with the longitudinal correlation function of the velocity in the x direction, and ν is the kinematic viscosity); N is the number of collocation points; Resolution is Δ/η (Δ is the grid size and η is the Kolmogorov scale); Taylor-based Reynolds number is $Re_\lambda = u_{rms}\lambda/\nu$ (λ is the Taylor length scale calculated with velocity fluctuations in the x direction); Ratio between rms velocity fluctuations in the x and z directions is u_{rms}/w_{rms}. The statistics are taken on the center plane of the shear-free turbulence.

Flow	Re_0	N	Δ/η	Re_λ	λ/η	L/η	u_{rms}/w_{rms}
SFT1	909	1024	1.3	192	27.3	126	1.04
SFT2	473	1024	1.1	126	22.1	89	0.96
SFT3	289	512	1.4	93	19.0	57	1.05

III. CONDITIONAL STATISTICS OF THE TURBULENT/NONTURBULENT INTERFACIAL LAYER

A. Detection of the outer edge of the turbulent/nonturbulent interfacial layer

It is useful to define the outer edge of the TNTI layer, called "irrotational boundary" [30], which represents an isosurface of vorticity magnitude $|\boldsymbol{\omega}| = \omega_{th}$. The threshold ω_{th} is determined by analyzing the volume of the turbulent region, defined by $|\boldsymbol{\omega}| > \omega_{th}$, as a function of ω_{th} as described in Ref. [31]. Since $|\boldsymbol{\omega}|$ rapidly changes across the thin TNTI layer, this isosurface location is insensitive to ω_{th} as long as ω_{th} is taken from an appropriate range [31–33]. At each point of the irrotational boundary, a local coordinate ζ_I, pointing in the normal direction of the irrotational boundary, is defined by a unit vector $\boldsymbol{n} = -\nabla\omega^2/|\nabla\omega^2|$. Here, $\zeta_I < 0$ and $\zeta_I > 0$ represent the turbulent and nonturbulent regions, respectively, while the irrotational boundary is at $\zeta_I = 0$. Figure 1 illustrates examples of the local coordinate. Here, the flow is visualized on a two-dimensional plane for an explanation while the local coordinate is defined with the three-dimensional vector $\boldsymbol{n}$. Using this local coordinate, averages conditioned on ζ_I can be obtained by averaging over points taken at the same distance ζ_I from the irrotational boundary, either in the turbulent or in the nonturbulent flow regions [3]. This average is denoted by $\langle\ \rangle_I$.

The procedure for computing the conditional statistics is the same as in Refs. [23,34]. The conditional statistics are calculated as functions of ζ_I by taking samples from the local coordinate assigned for various locations on the isosurface of $|\boldsymbol{\omega}| = \omega_{th}$. Each local coordinate is discretized with spacing close to the Kolmogorov scale η taken at the center of the shear-free turbulence, and variables on the DNS grids are interpolated onto the discrete points of the local coordinate

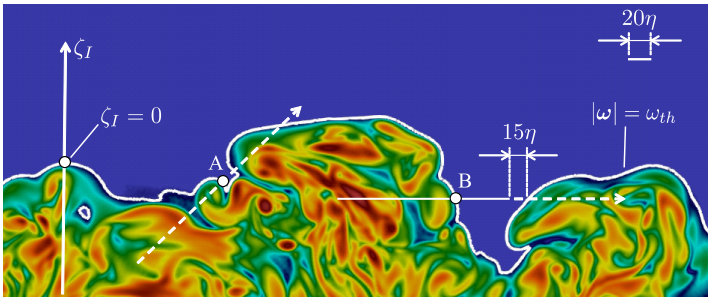

FIG. 1. Local coordinate ζ_I used for calculating conditional statistics. A color represents $\log_{10}(\boldsymbol{\omega}\cdot\boldsymbol{\omega})$ while an isosurface of $|\boldsymbol{\omega}| = \omega_{th}$ is shown with white lines (SFT1). The coordinates shown with broken lines are excluded from samples of conditional statistics.

with the trilinear interpolation. The local coordinate sometimes crosses the isosurface more than once. The conditional statistics are calculated separately in turbulent and nonturbulent regions by excluding some of the local coordinates from statistical samples, as explained below. The local coordinates shown with broken lines in Fig. 1 are not used for the conditional statistics. When the local coordinate crosses another point of $|\boldsymbol{\omega}| = \omega_{th}$ for $|\zeta_I| \leqslant 15\eta$, the entire local coordinate is excluded from the analysis. This example is shown as A in Fig. 1. When the local coordinate crosses another point of $|\boldsymbol{\omega}| = \omega_{th}$ for $|\zeta_I| > 15\eta$ (shown as B), the region within a distance of 15η from $|\boldsymbol{\omega}| = \omega_{th}$ is excluded from the conditional statistics. Here, 15η is determined from the thickness of the TNTI layer, and it was confirmed that the conditional statistics do not depend on this length [34]. In this way, the turbulent and nonturbulent regions which appear in $\zeta_I > 0$ and $\zeta_I < 0$, respectively, are excluded from samples of the conditional statistics, and the conditional statistics at a given ζ_I are calculated solely from turbulent or nonturbulent regions. The number of points on the irrotational boundary used for setting the local coordinate affects the convergence of the conditional statistics, as examined in Appendix A. Here, the spacing between the two nearby points used as the origins of ζ_I is less than 10η.

B. Scale decomposition of kinetic energy

We consider the kinetic energy of the flow as a function of a length scale r, where the scale separation is achieved by using a low-pass filter [26]. The filtering operation at a given scale r is defined as a volume average made in a sphere of radius r, centered at a point $\boldsymbol{x}$, with volume $V_R(r)$. Specifically, we define the average of any given function $\phi(\boldsymbol{x}, t)$ within the spherical volume of radius r as

$$\overline{\phi}(\boldsymbol{x}, t, r) = \frac{\iiint G(\boldsymbol{x}, \boldsymbol{x}', r)\phi(\boldsymbol{x}', t)d\boldsymbol{x}'}{V_R}, \tag{1}$$

where G is a kernel function which is equal to 1 and 0 inside ($|\boldsymbol{x} - \boldsymbol{x}'| \leqslant r$) and outside ($|\boldsymbol{x} - \boldsymbol{x}'| > r$) the sphere, respectively. The volume is calculated as $V_R = \iiint G(\boldsymbol{x}, \boldsymbol{x}', r)d\boldsymbol{x}'$. Therefore, Eq. (1) is equivalent to the top-hat filter. The kinetic energy of the fluid contained in scales smaller than r can be represented as $k_r(\boldsymbol{x}, t, r) = \overline{u_i u_i}/2 - \overline{u_i}\,\overline{u_i}/2$. Following studies on the subgrid scale (SGS) energy budget [35,36], the governing equation for k_r is written as

$$\frac{\partial k_r}{\partial t} + \overline{u_j}\frac{\partial k_r}{\partial x_j} = D_P + D_\nu + D_T + D_S + \varepsilon_\nu + \Pi, \tag{2}$$

with

$$D_P = \frac{\partial}{\partial x_j}(\overline{p}\,\overline{u_j} - \overline{pu_j}) = -\overline{u_j\frac{\partial p}{\partial x_j}} + \overline{u_j}\,\overline{\frac{\partial p}{\partial x_j}}, \tag{3}$$

$$D_\nu = \frac{\nu}{2}\frac{\partial^2}{\partial x_j \partial x_j}(\overline{u_i u_i} - \overline{u_i}\,\overline{u_i}) = \nu\left(\frac{1}{2}\overline{\frac{\partial^2 u_i u_i}{\partial x_j \partial x_j}} - \overline{\frac{\partial u_i}{\partial x_j}}\,\overline{\frac{\partial u_i}{\partial x_j}} - \overline{u_i}\,\overline{\frac{\partial^2 u_i}{\partial x_j \partial x_j}}\right), \tag{4}$$

$$D_T = \frac{1}{2}\frac{\partial}{\partial x_j}(\overline{u_i u_i}\,\overline{u_j} - \overline{u_i u_i u_j}) = -\overline{u_i u_j\frac{\partial u_i}{\partial x_j}} + \overline{u_j}\,\overline{u_i\frac{\partial u_i}{\partial x_j}}, \tag{5}$$

$$D_S = \frac{\partial}{\partial x_j}[(\overline{u_i u_j} - \overline{u_i}\,\overline{u_j})\overline{u_i}] = \overline{u_i}\,\overline{u_j\frac{\partial u_i}{\partial x_j}} - \overline{u_i}\,\overline{u_j}\,\overline{\frac{\partial u_i}{\partial x_j}} + (\overline{u_i u_j} - \overline{u_i}\,\overline{u_j})\overline{\frac{\partial u_i}{\partial x_j}}, \tag{6}$$

$$\varepsilon_\nu = -\nu\left[\overline{\frac{\partial u_i}{\partial x_j}\frac{\partial u_i}{\partial x_j}} - \overline{\frac{\partial u_i}{\partial x_j}}\,\overline{\frac{\partial u_i}{\partial x_j}}\right], \tag{7}$$

$$\Pi = -(\overline{u_i u_j} - \overline{u_i}\,\overline{u_j})\overline{\frac{\partial u_i}{\partial x_j}}. \tag{8}$$

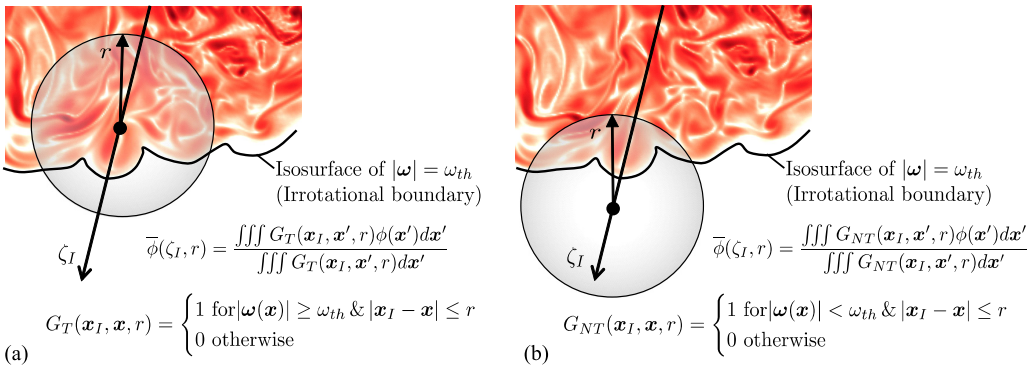

FIG. 2. Sketch outlining the computation of the conditional spherical averaging for spheres whose center is located in (a) the turbulent region and (b) the nonturbulent region. The position on the interface coordinate ζ_I is denoted by $\boldsymbol{x}_I$ in the global coordinate system.

Here, D_P is the pressure diffusion, D_ν is the viscous diffusion, D_T is the turbulent diffusion, D_S is the diffusive effects arising from the interaction between the large-scale velocity $\overline{u_i}$ and the small-scale stress tensor $\overline{u_i u_j} - \overline{u_i}\,\overline{u_j}$, ε_ν is the viscous dissipation, and Π represents the interscale energy transfer between large and small scales. All terms are expressed in forms that do not contain spatial derivatives of filtered quantities and fluctuations for application of this equation near the TNTI layer explained below.

To study the scale-by-scale kinetic energy budget in relation to the TNTI layer, the volume averaging procedure is combined with conditional averages computed in relation to the interface position. Figure 2 outlines the procedure used for combining the spherical volume average with the conditional average on ζ_I. The computation of Eq. (1) raises no particular difficulty when the flow region within the volume is totally in the turbulent (or the nonturbulent) region. However, the procedure needs to be slightly modified near the TNTI layer for studying separately the turbulent and the nonturbulent flow regions. The volume average is defined with a sphere of radius r whose center is located at $\boldsymbol{x}_I$, which is also located at ζ_I on the interface coordinate as sketched in Fig. 2. The present method uses kernel functions G_T and G_{NT} that can assume 0 or 1 depending on the position of the flow point $\boldsymbol{x}$ and the center of the sphere $\boldsymbol{x}_I$ as defined in Fig. 2. Turbulent and nonturbulent regions are identified on each side of the irrotational boundary. Therefore, the filter defined with G_T or G_{NT} works as the volume average of the turbulent or nonturbulent regions.

The following procedure is adapted for calculating the conditional statistics of filtered quantities: We consider a point on the isosurface of $|\boldsymbol{\omega}| = \omega_{th}$ whose location is given by $\boldsymbol{x}_\omega = \boldsymbol{x}_{\omega 1}$ in the Cartesian coordinate system. For $\boldsymbol{x}_\omega = \boldsymbol{x}_{\omega 1}$ on the isosurface, the local coordinate ζ_I is defined. At one point on the local coordinate denoted as $\zeta_I = \zeta_{I1}$, the function G_T or G_{NT} for a given filter length $r = r_1$ is defined based on the profile of $|\boldsymbol{\omega}(x, y, z)|$ and $|\boldsymbol{\omega}|$ at $\zeta_I = \zeta_{I1}$, as explained in Fig. 2. Equation (2) is valid for this filter defined with $(\boldsymbol{x}_\omega, \zeta_I, r) = (\boldsymbol{x}_{\omega 1}, \zeta_{I1}, r_1)$ because the same filter is applied in the entire computational domain. At $\zeta_I = \zeta_{I1}$, we calculate the filtered quantities, e.g., k_r and Eq. (2), which are used as samples of conditional statistics at $\zeta_I = \zeta_{I1}$. This procedure is repeated for different sets of $(\boldsymbol{x}_\omega, \zeta_I, r)$. Finally, the conditional statistics of filtered quantities are obtained as functions of (ζ_I, r) by taking ensemble averages of different $\boldsymbol{x}_\omega$. Because Eqs. (3)–(8) are written in forms that do not contain the derivative of filtered quantities, filtered values for the filter defined with $(\boldsymbol{x}_\omega, \zeta_I, r) = (\boldsymbol{x}_{\omega 1}, \zeta_{I1}, r_1)$ are calculated only at $\zeta_I = \zeta_{I1}$, and they are used for calculating the conditional statistics. This method requires the filter calculation only at $\zeta_I = \zeta_{I1}$ instead of the entire computational domain, and significantly reduces the computational cost of the conditional analysis of Eqs. (3)–(8).

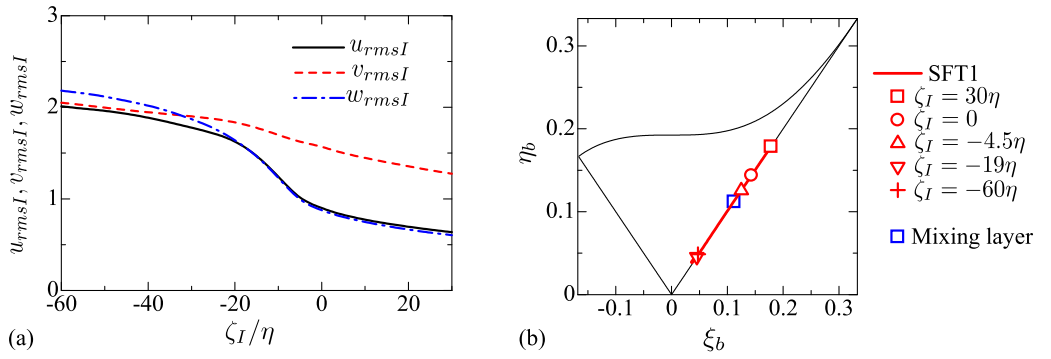

FIG. 3. (a) Conditional rms velocity fluctuations in SFT1. (b) Variation of ξ_b and η_b across the TNTI layer in SFT1. (ξ_b, η_b) obtained at the center of a fully developed turbulent mixing layer [38] is also plotted for comparison. Three thin lines in panel (b) correspond to an axisymmetric state with one large eigenvalue, $\eta_b = \xi_b$, or one small eigenvalue, $\eta_b = -\xi_b$, and a two-dimensional state $\eta_b = (1/27 + 2\xi_b^3)^{1/2}$.

IV. RESULTS AND DISCUSSION

A. Conditional statistics near the turbulent/nonturbulent interfacial layer

The present work mainly relies on results obtained with SFT1 while SFT2 and SFT3 are used to examine the Reynolds-number dependence. The Kolmogorov scale at the center of the shear-free turbulence ($y = 0$) is used to normalize the distance ζ_I and scale r in the plots of conditional statistics. It should be noted that the Kolmogorov scale in the turbulent region hardly depends on the transverse position except within the TNTI layer [34]. The TNTI layer can be defined as a buffer layer where the vorticity magnitude is adjusted between the turbulent and nonturbulent regions [1]. Based on the mean vorticity magnitude conditioned on ζ_I, the TNTI layer is found to be located for $-19\eta \lesssim \zeta_I \leqslant 0$ in the present DNS, where the reference Kolmogorov scale η is computed at the center of the shear-free turbulence. Two sublayers within the TNTI layer can be defined based on vorticity dynamics. One is called a viscous superlayer (VSL) and appears at the outer part of the TNTI layer, where enstrophy growth is dominated by viscous diffusion [7,9,37]. The other one is a turbulent sublayer (TSL) and is a buffer layer located between the viscous superlayer and the turbulent core region. In the TSL, vortex stretching has an important contribution to enstrophy growth [1]. The VSL and TSL are detected by examining the enstrophy budget near the TNTI layer, and are found for $-4.3\eta \leqslant \zeta_I \leqslant 0$ and $-19\eta \leqslant \zeta_I \leqslant -4.3\eta$, respectively, in SFT1. The turbulent region inside the TNTI layer is called a turbulent core region in this paper. Further details of the identification of the TNTI layer and sublayers in the shear-free turbulence are described in Ref. [23].

Figure 3(a) shows rms velocity fluctuations near the TNTI layer. For the x direction, the rms velocity fluctuation is defined as $u_{rmsI} = (\langle u^2 \rangle_I - \langle u \rangle_I^2)^{1/2}$, and those in other directions are defined in the same manner. In the turbulent core region ($\zeta_I \lesssim -20\eta$), rms velocity fluctuations are similar for all components. Within the TNTI layer ($-20\eta \lesssim \zeta_I \leqslant 0$), u_{rmsI} and w_{rmsI} decrease toward the nonturbulent region while the decrease of v_{rmsI} is much slower than the other components. Therefore, the velocity fluctuations are more anisotropic within the TNTI layer and in the nonturbulent region than in the turbulent core region. The nonturbulent region has large velocity fluctuations in the y direction, which is the direction of the mean flow development. This result is consistent with the conditional rms velocity fluctuations in a turbulent planar jet, where velocity fluctuations are larger in the lateral direction than in the spanwise direction [39]. With the Reynolds stress tensor defined with the conditional averages, $R_{ij} = \langle u_i u_j \rangle_I - \langle u_i \rangle_I \langle u_j \rangle_I$, the normalized anisotropy tensor can be defined as

$$b_{ij} = \frac{R_{ij}}{R_{kk}} - \frac{1}{3}\delta_{ij}, \tag{9}$$

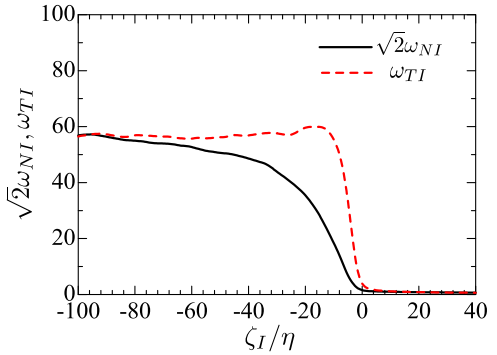

FIG. 4. Conditional rms vorticity in normal and tangential directions of the irrotational boundary: $\sqrt{2}\omega_{NI} = \sqrt{2}\langle\omega_N^2\rangle_I^{1/2}$ and $\omega_{TI} = \langle\omega_T^2\rangle_I$ with $\omega_N = \boldsymbol{n}\cdot\boldsymbol{\omega}$ and $\omega_T^2 = \omega^2 - \omega_N^2$.

where δ_{ij} is the Kronecker delta. The state of anisotropy of the Reynolds stress tensor is often expressed with $\eta_b = (b_{ij}b_{ji}/6)^{1/2}$ and $\xi_b = (b_{ij}b_{jk}b_{ki}/6)^{1/3}$, which are related to the invariants of b_{ij} [40]. Figure 3(b) shows variations of η_b and ξ_b for $-60\eta \leqslant \zeta_I \leqslant 30\eta$ on the plane of ξ_b and η_b. The figure also shows the result obtained at the center of the fully developed mixing layer, where the Reynolds stress is calculated with conventional time averages instead of conditional averages [38]. From the nonturbulent to turbulent region, the state of anisotropy changes from $(\xi_b, \eta_b) \approx (0.2, 0.2)$ to (0.05,0.05) and approaches the isotropic state $(\xi_b, \eta_b) = (0, 0)$. Here, $(\xi_b, \eta_b) \approx (0.05, 0.05)$ is already achieved just at the end of the TNTI layer in the turbulent region ($\zeta_I = -19\eta$), and the Reynolds stress tensor in the turbulent region becomes anisotropic within the TNTI layer. It should be noted that the center of the mixing layer is more anisotropic than the turbulent region of the shear-free turbulence because the shear-free turbulence does not have a mean velocity gradient.

On the local coordinate taken in the $\boldsymbol{n}$ direction, the vorticity component in the $\boldsymbol{n}$ direction is given by $\omega_N = \boldsymbol{n}\cdot\boldsymbol{\omega}$. On the other hand, $\omega_T^2 = \omega^2 - \omega_N^2$ represents a contribution to $\omega^2 = \boldsymbol{\omega}\cdot\boldsymbol{\omega}$ from the vorticity components in the tangential direction of the irrotational boundary. Figure 4 shows the conditional rms vorticities in the normal and tangential directions, which are defined as $\omega_{NI} = \langle\omega_N^2\rangle_I^{1/2}$ and $\omega_{TI} = \langle\omega_T^2\rangle_I^{1/2}$. In the figure, ω_{NI} is multiplied by $\sqrt{2}$ because ω_{TI} is equal to $\sqrt{2}\omega_{NI}$ when $\langle\omega_x^2\rangle_I = \langle\omega_y^2\rangle_I = \langle\omega_z^2\rangle_I$. Although ω_{TI} sharply decreases for $10\eta \lesssim \zeta_I \leqslant 0$, ω_{NI} decreases slowly from the turbulent core region toward the nonturbulent region. This is because the vorticity vector near the TNTI layer is mostly oriented in the tangential direction to the interface [33,41]. The isotropic relation $\sqrt{2}\omega_{NI} \approx \omega_{TI}$ is still valid in the turbulent core region of $\zeta_I \lesssim 50\eta$ although the presence of the TNTI layer affects the vorticity field within and near the TNTI layer of the shear-free turbulence.

B. Scale-by-scale energy budget near the turbulent/nonturbulent interfacial layer

The filter defined with G_T or G_{NT} excludes some regions from the volume average. Therefore, the properties of the filter change upon introducing G_T or G_{NT}. Here, the effective cutoff length becomes smaller than the original filter. The characteristic length of the filter is estimated as

$$R_f = \left[\frac{3}{4\pi}\iiint G(\boldsymbol{x}_I, \boldsymbol{x}', r)d\boldsymbol{x}'\right]^{1/3}, \tag{10}$$

with $G = G_T$ or G_{NT}. With this definition, R_f is equal to r for the conventional top-hat filter, for which $G(\boldsymbol{x}_I, \boldsymbol{x}, r) = 1$ for $|\boldsymbol{x}_I - \boldsymbol{x}| \leqslant r$ and $G = 0$ for $|\boldsymbol{x}_I - \boldsymbol{x}| > r$. R_f can be treated as a variable on the local coordinate, and the conditional average of R_f divided by r is plotted as a function of $(r/\eta, \zeta_I/\eta)$ in Fig. 5(a). For small r, $\langle R_f\rangle_I/r = 1$ is obtained for most ζ_I, and the filter length is not different from r, which is used for plotting the conditional statistics in this study. However,

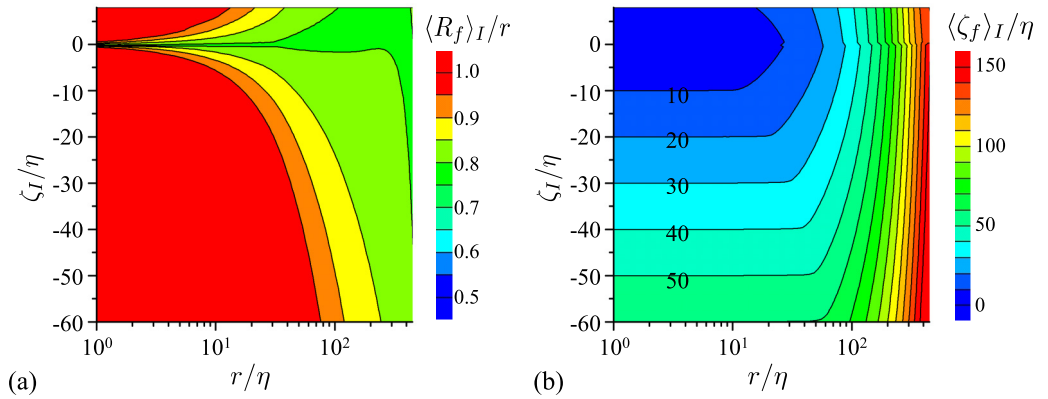

FIG. 5. Properties of the filter used near the TNTI layer: (a) the effective filter size $\langle R_f\rangle_I$ divided by r; (b) the location $\langle\zeta_f\rangle_I$ at which filtered quantities are defined. These results are taken from SFT1.

$\langle R_f\rangle_I/r$ decreases with r especially for small ζ_I, and the cutoff length of the filter at large scales is not accurately represented by r. A similar issue also arises for the location ζ_I at which the filtered quantities are defined since the center of the filter changes upon introducing G_T or G_{NT}. The location where the filtered quantities are defined is estimated as the mass center of the volume used for defining the volume average and is given by

$$\boldsymbol{x}_f = \frac{\iiint \boldsymbol{x}' G(\boldsymbol{x}_I, \boldsymbol{x}', r) d\boldsymbol{x}'}{\iiint G(\boldsymbol{x}_I, \boldsymbol{x}', r) d\boldsymbol{x}'}, \tag{11}$$

with $G = G_T$ or G_{NT}. The distance from the origin of the local coordinate ($\zeta_I = 0$) to $\boldsymbol{x}_f$ is denoted ζ_f. Figure 5(b) shows the conditional average of ζ_f divided by η, where $\langle\zeta_f\rangle_I = |\zeta_I|$ appears as horizontal lines. The filtered quantities are defined at ζ_I without any problems when $\langle\zeta_f\rangle_I = |\zeta_I|$, which is observed for small r. $\langle\zeta_f\rangle_I$ tends to be larger than $|\zeta_I|$ for large r. In this case, the conditional statistics do not represent the properties of turbulence at ζ_I. Therefore, the conditional statistics are presented for $|\zeta_I| \geqslant r$ in the rest of the paper.

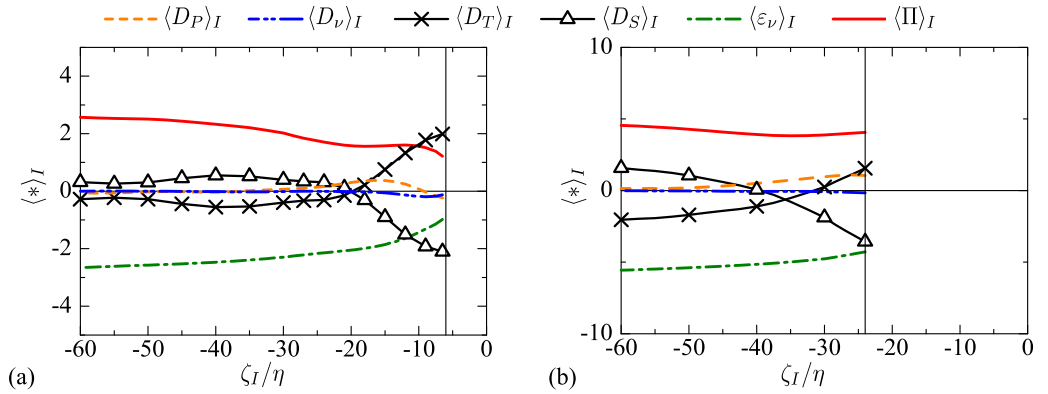

FIG. 6. Cumulative kinetic energy budgets as functions of ζ_I/η for SFT1, showing all the terms in Eq. (2), i.e., pressure diffusion $\langle D_P\rangle_I$, viscous diffusion $\langle D_\nu\rangle_I$, turbulent diffusion $\langle D_T\rangle_I$, diffusion by large- and small-scale interactions $\langle D_S\rangle_I$, viscous dissipation $\langle\varepsilon_\nu\rangle_I$, and energy flux $\langle\Pi\rangle_I$ for (a) $r = 6\eta$ and (b) $r = 24\eta$. The results are presented for $|\zeta_I| \geqslant r$.

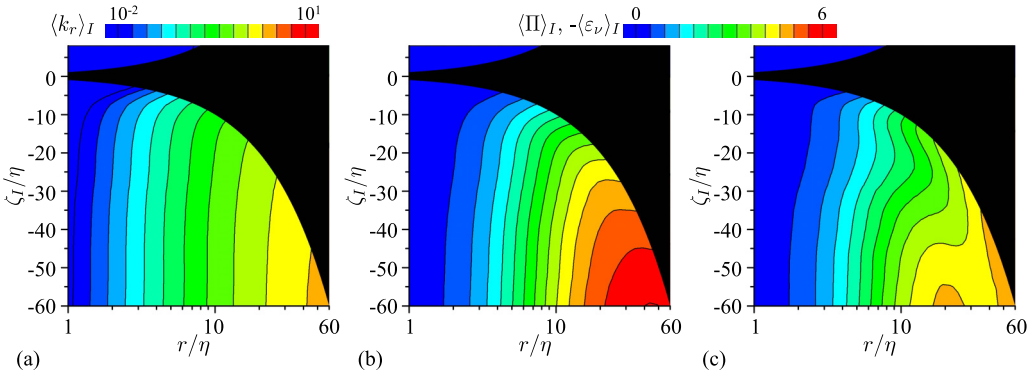

FIG. 7. (a) Cumulative kinetic energy near the TNTI layer and conditional averages of (b) viscous dissipation $-\langle \varepsilon_v \rangle_I$ and (c) energy flux $\langle \Pi \rangle_I$, which are plotted as functions of ζ_I and r in SFT1. Black regions represents $|\zeta_I| < r$.

Figure 6 shows the cumulative kinetic energy budgets in the turbulent region near the TNTI layer in SFT1 for two different scales ($r = 6\eta$ and 24η), showing conditional averages of all the terms in Eq. (2) as functions of ζ_I. These budgets are quite different from the classical kinetic energy budgets in free shear flows. The transport terms D_T and D_S are more important near the irrotational boundary than in the turbulent core region. Far from the TNTI layer, the mean energy flux $\langle \Pi \rangle_I$ roughly balances the mean viscous dissipation $\langle \varepsilon_v \rangle_I$ for both length scales $r = 6\eta$ and 24η. The viscous diffusion $\langle D_v \rangle_I$ is always negligible near the TNTI layer at $r = 24\eta$. However, $\langle D_v \rangle_I$ at $r = 6\eta$ becomes negative within the TNTI layer, indicating the energy transfer from the TSL to the VSL (this is further confirmed by positive $\langle D_v \rangle_I$ in the VSL in Fig. 9). The pressure diffusion $\langle D_P \rangle_I$ displays an oscillation within the TNTI layer for $r = 6\eta$ while negative $\langle D_P \rangle_I$ cannot be observed at $r = 24\eta$.

Figure 7(a) displays the conditional profile of the cumulative kinetic energy $\langle k_r \rangle_I$ as a function of both r and ζ_I. This plot confirms that there is less energy at small scales in the nonturbulent region ($\zeta_I > 0$) than in the turbulent region ($\zeta_I < 0$). $\langle k_r \rangle_I$ hardly depends on ζ_I for $\zeta_I/\eta \lesssim -15$, i.e., in the turbulent core region. However, $\langle k_r \rangle_I$ at small scales $r/\eta \lesssim 10$ decreases as the irrotational boundary (located at $\zeta_I = 0$) is approached from the turbulent region. The decrease of $\langle k_r \rangle_I$ at small scales is more important within the VSL ($-4\eta \lesssim \zeta_I \leqslant 0$) than in the TSL ($-19\eta \lesssim \zeta_I \lesssim -4\eta$). This confirms one of the key assumptions made in previous studies and models of the TNTI layer [42,43]; namely, that the TNTI layer inhibits the buildup of small-scale turbulent motions. Small-scale velocity fluctuations are small in the VSL and the nonturbulent regions because the kinetic energy in these regions is associated with large-scale motions, which can also contribute to the irrotational strain near the TNTI layer [8,44,45]. Therefore, the rms velocity fluctuations in Fig. 3 are not negligible in the VSL and the nonturbulent regions because the rms fluctuations contain the contributions from all length scales.

Figures 7(b) and 7(c) show conditional averages of the viscous dissipation $-\langle \varepsilon_v \rangle_I$ and the interscale energy flux $\langle \Pi \rangle_I$ in Eq. (2), respectively. The separation between the turbulent and nonturbulent regions is also clearly observed because the dissipation and the energy flux are very small in the nonturbulent region. The magnitude of the dissipation increases with r. Both $-\langle \varepsilon_v \rangle_I$ and $\langle \Pi \rangle_I$ at small scales become small as the irrotational boundary is approached from the turbulent region. Figures 7(b) and 7(c) confirm that the interscale energy transfer to very small scales as well as the dissipation at small scales are both suppressed within the VSL. Appendix B presents the cumulative kinetic energy and the mean interscale energy flux obtained with a conventional filter that does not distinguish turbulent and nonturbulent regions.

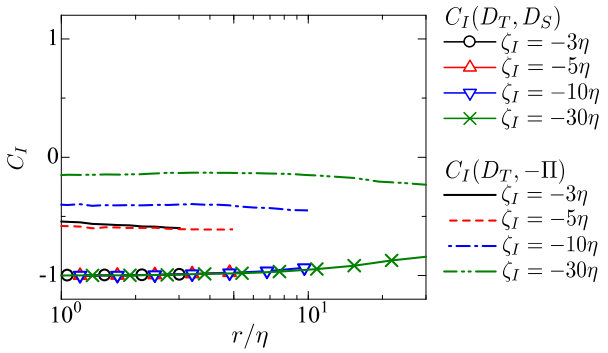

FIG. 8. Correlation coefficients between D_T and D_S, $C_I(D_T, D_S)$, and between $-\Pi$ and D_T, $C_I(D_T, -\Pi)$, plotted against r/η in SFT1. The results are presented for $|\zeta_I| \geqslant r$.

Returning to Fig. 6, one of the most interesting features concerns the turbulent diffusion $\langle D_T \rangle_I$ and the diffusion by large- and small-scale interactions $\langle D_S \rangle_I$, both of which become large in magnitude as the irrotational boundary is approached. The profiles of $\langle D_T \rangle_I$ and $\langle D_S \rangle_I$ suggest that they are in some sort of balance, partially canceling their global effect. Their signs change upon approaching the irrotational boundary from the turbulent region. For instance, the turbulent diffusion $\langle D_T \rangle_I$ changes from negative to positive values as the irrotational boundary is approached. Thus, the turbulent diffusion removes kinetic energy from the core of the turbulent flow and feeds that energy into a fluid near the TNTI layer. The opposite effect (sign) can be seen for $\langle D_S \rangle_I$. Figure 6 shows that the point where the signs of these terms change is clearly outside the TNTI layer for $r = 24\eta$, implying large-scale effects on these terms. Both $\langle D_T \rangle_I$ and $\langle D_S \rangle_I$ change their sign closer to the irrotational boundary as the scale decreases (at $\zeta_I/\eta \approx -35$ for $r = 24\eta$ and $\zeta_I/\eta \approx -20$ for $r = 6\eta$). Notice that both terms become even more important than $\langle \Pi \rangle_I$ and $\langle \varepsilon_v \rangle_I$ near the irrotational boundary for $r = 6\eta$. The link between D_T and D_S becomes even clearer when analyzing the correlation between the two quantities at several scales. Figure 8 shows the correlation coefficient between these terms. The distance from the irrotational boundary does not affect the degree of (anti) correlation between the two quantities, which is very high in the entire TNTI layer. In Eq. (6), the last term of D_S is equal to $-\Pi$. The analysis with the Kármán-Howarth-Monin-Hill equation indicates that Π and D_T are correlated with each other in a turbulent wake [46], and this correlation can be the reason for the anticorrelation between D_T and D_S. This is examined by calculating the correlation coefficient between D_T and $-\Pi$, which is also shown in Fig. 8. Although D_T and $-\Pi$ are negatively correlated, the correlation is not strong enough to cause the strong anticorrelation between D_T and D_S. The correlation between D_T and $-\Pi$ is stronger within the TNTI layer than in the turbulent core region. The correlation between D_T and $-\Pi$ was also found in the near field of the wake, where the flow is highly anisotropic and inhomogeneous [46].

The conditional averages of the remaining terms in Eq. (2) are shown in Fig. 9, where $\langle D_S \rangle_I$ is not shown because it strongly resembles the profile of D_T with an opposite sign. The pressure diffusion $\langle D_P \rangle_I$ [Fig. 9(a)] is mostly positive for $\zeta_I/\eta \leqslant -10$, and tends to increase the kinetic energy of the flow near the TNTI layer. However, $\langle D_P \rangle_I$ is negative for small scales at $\zeta_I/\eta \approx -5$, and the small-scale kinetic energy is removed by the pressure effect within the TNTI layer. On the other hand, the mean viscous diffusion in Fig. 9(b) is small compared with the other terms. However, it locally removes energy from the turbulent region while it contributes to the kinetic energy growth in the VSL region at small scales. The separation between positive and negative values of $\langle D_v \rangle_I$ and $\langle D_P \rangle_I$ seems to occur within the TNTI layer, which suggests that the role of the pressure and viscous forces in the kinetic energy transfer is affected by the presence of the TNTI layer. It has also been shown that the viscous diffusion transfers enstrophy from the TSL toward the VSL [7,37]. The profile of $\langle D_v \rangle_I$ indicates that the viscous diffusion for the kinetic energy also has a similar role at

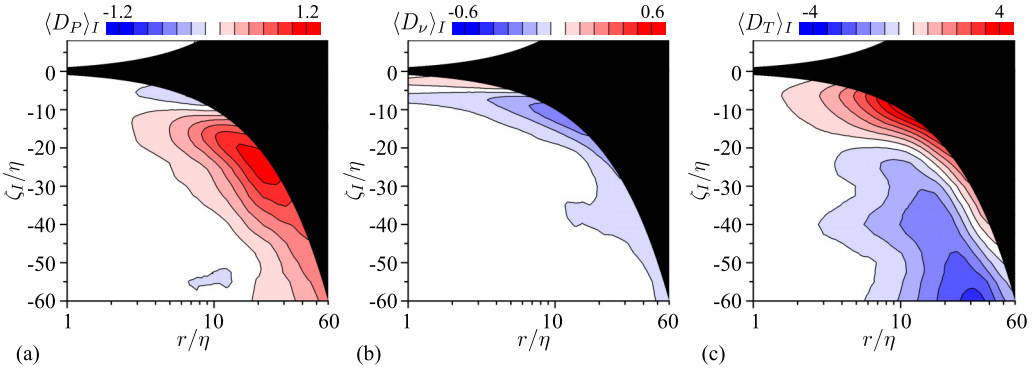

FIG. 9. Conditional averages of diffusion terms of the cumulative kinetic energy as functions of ζ_I and r in SFT1: (a) pressure diffusion $\langle D_P\rangle_I$; (b) viscous diffusion $\langle D_\nu\rangle_I$; (c) turbulent diffusion $\langle D_T\rangle_I$. The results are presented for $|\zeta_I| \geqslant r$ while black represents $|\zeta_I| < r$.

small scales $r \lesssim 6\eta$, and the viscous diffusion of enstrophy within the TNTI layer can be associated with the kinetic energy diffusion at the small scales. $\langle D_T\rangle_I$ shown in Fig. 9(c) is positive within and near the TNTI layer, while it becomes negative far from the TNTI layer. Thus, $\langle D_T\rangle_I$ does not seem to be correlated with the pressure diffusion $\langle D_P\rangle_I$ or the viscous diffusion $\langle D_\nu\rangle_I$, and it transfers the energy toward the region near the TNTI layer from the turbulent core region.

C. Pressure diffusion at small scales within the turbulent/nonturbulent interfacial layer

In Fig. 9(a), the pressure diffusion term displays negative values near the TNTI layer. The minimum value of the pressure diffusion within the TNTI layer is examined with the three simulations used in this work. Figure 10(a) shows the location ζ_I and scale r of the minimum as a function of the Reynolds number. The minimum of $\langle D_P\rangle_I$ is obtained at $(r,\ \zeta_I) \approx (5.8\eta,\ -6.0\eta)$, which is relatively independent of the Reynolds number. Thus, the pressure diffusion D_P effectively reduces the kinetic energy at small scales around $\zeta_I = -6\eta$, i.e., within the TSL region. Since both the pressure diffusion D_P and the viscous dissipation ε_ν reduce the kinetic energy within this layer, Fig. 10(b) shows their relative importance, compared with the energy flux, as a function of the

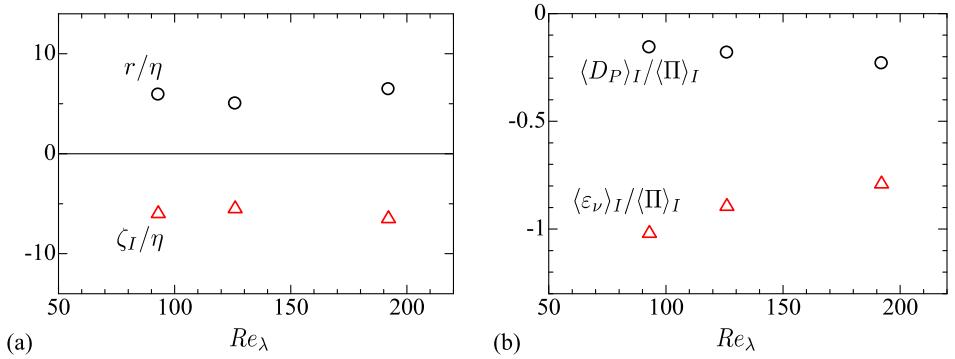

FIG. 10. (a) Coordinate within the TNTI layer (ζ_I/η) and scale (r/η) at which the mean pressure diffusion term $\langle D_P\rangle_I$ attains its minimum, plotted against the Reynolds number on the centerline of the shear-free turbulence. (b) Comparison between the mean pressure diffusion $\langle D_P\rangle_I$ and the energy dissipation $\langle\varepsilon_\nu\rangle_I$ (both normalized by the energy flux $\langle\Pi\rangle_I$) plotted against the Reynolds number, where the values are taken from the locations where $\langle D_p\rangle_I$ attains its minimum shown in panel (a).

Reynolds number. In all cases, $\langle \varepsilon_\nu \rangle_I$ is more important than $\langle D_P \rangle_I$. However, as the Reynolds number increases, the magnitude of $\langle D_P \rangle_I / \langle \Pi \rangle_I$ slightly increases, and conversely $\langle \varepsilon_\nu \rangle_I / \langle \Pi \rangle_I$ decreases. Even though $\langle \varepsilon_\nu \rangle_I$ remains dominant, $\langle D_P \rangle_I$ is not negligible and accounts for roughly 20% of the total kinetic energy transferred for the scale of $r \approx 6\eta$.

The local minimum value of $\langle D_P \rangle_I$ in the vicinity of its positive values for small scales is possibly explained by the presence of small-scale vortices within the TNTI layer. A previous DNS study on the SGS kinetic energy transfer observed that negative peaks of D_P are often centered at the vortex cores, which are surrounded by positive D_P [36]. It has also been shown that small-scale vortices with a radius of about 5η frequently appear within the TSL [32,41,47]. The outer edge of the TNTI layer is formed around these vortices near the edge of the turbulent region, as visualized in previous studies [32,33,41], and the local coordinate in the interface normal direction often crosses the core of the vortices. Therefore, the small-scale vortices within the TSL can cause the local minimum of $\langle D_P \rangle_I$ at small scales within the TSL and positive $\langle D_P \rangle_I$ around there.

D. Interscale energy transfer near the turbulent/nonturbulent interfacial layer

The interscale energy flux Π is further examined with the velocity vector and gradient described in relation to the interface orientation. On each local coordinate ζ_I, we can define the orthogonal coordinate system (ζ_I, ζ_{t1}, ζ_{t2}), where ζ_{t1} and ζ_{t2} are the coordinates in tangential directions of the irrotational boundary. Here, tangential directions are arbitrary on the plane perpendicular to the interface normal direction $\boldsymbol{n}$. The velocity components in the ζ_I, ζ_{t1}, and ζ_{t2} directions are denoted by u_n, u_{t1}, and u_{t2}, respectively. With these velocity components, Π is decomposed as

$$\Pi = \Pi_{n,n} + \Pi_{n,t} + \Pi_{t,n} + \Pi_{t,tl} + \Pi_{t,tt}, \tag{12}$$

$$\Pi_{n,n} = -(\overline{u_n u_n} - \overline{u_n}\,\overline{u_n})\overline{\frac{\partial u_n}{\partial \zeta_I}}, \tag{13}$$

$$\Pi_{n,t} = -(\overline{u_n u_{t1}} - \overline{u_n}\,\overline{u_{t1}})\overline{\frac{\partial u_n}{\partial \zeta_{t1}}} - (\overline{u_n u_{t2}} - \overline{u_n}\,\overline{u_{t2}})\overline{\frac{\partial u_n}{\partial \zeta_{t2}}}, \tag{14}$$

$$\Pi_{t,n} = -(\overline{u_{t1} u_n} - \overline{u_{t1}}\,\overline{u_n})\overline{\frac{\partial u_{t1}}{\partial \zeta_I}} - (\overline{u_{t2} u_n} - \overline{u_{t2}}\,\overline{u_n})\overline{\frac{\partial u_{t2}}{\partial \zeta_I}}, \tag{15}$$

$$\Pi_{t,tl} = -(\overline{u_{t1} u_{t1}} - \overline{u_{t1}}\,\overline{u_{t1}})\overline{\frac{\partial u_{t1}}{\partial \zeta_{t1}}} - (\overline{u_{t2} u_{t2}} - \overline{u_{t2}}\,\overline{u_{t2}})\overline{\frac{\partial u_{t2}}{\partial \zeta_{t2}}}, \tag{16}$$

$$\Pi_{t,tt} = -(\overline{u_{t1} u_{t2}} - \overline{u_{t1}}\,\overline{u_{t2}})\overline{\frac{\partial u_{t1}}{\partial \zeta_{t2}}} - (\overline{u_{t2} u_{t1}} - \overline{u_{t2}}\,\overline{u_{t1}})\overline{\frac{\partial u_{t2}}{\partial \zeta_{t1}}}. \tag{17}$$

The decomposition only considers the sum of the contributions from t_1 and t_2 and does not take into account the dependence on specific directions on the tangential plane of the interface. $\Pi_{\alpha,\beta}$ represents the energy flux arising from the derivative of α-directional velocity with respect to the β direction, where the subscripts n and t denote the normal and tangential directions of the interface, respectively. $\Pi_{t,tl}$ contains the tangential velocity and its longitudinal derivative in the tangential direction, while $\Pi_{t,tt}$ contains the transverse derivative. Figure 11(a) shows the conditional averages of the decomposed terms with the length scale of $r/\eta = 6$. Averages of $\Pi_{n,n}$ and $\Pi_{t,n}$ have large positive values near the interface. These components contain the velocity gradient in the interface normal direction, and the energy transfer from large to small scales is caused by the gradient in the interface normal direction. On the contrary, the terms with the tangential gradient, $\Pi_{n,t}$ and $\Pi_{t,tl}$, have negative mean values near the interface, and these terms contribute to the mean energy transfer from small to large scales. However, the magnitudes of $\langle \Pi_{n,t} \rangle_I$ and $\langle \Pi_{t,tl} \rangle_I$ are smaller than $\langle \Pi_{n,n} \rangle_I$ and $\langle \Pi_{t,n} \rangle_I$, and the average of Π is still positive. The dependence on these directions is much weaker in the turbulent core region, and there are no significant influences of the TNTI on Π far away from the TNTI layer. Figure 11(b) shows the results at $r/\eta = 24$. The profiles of each

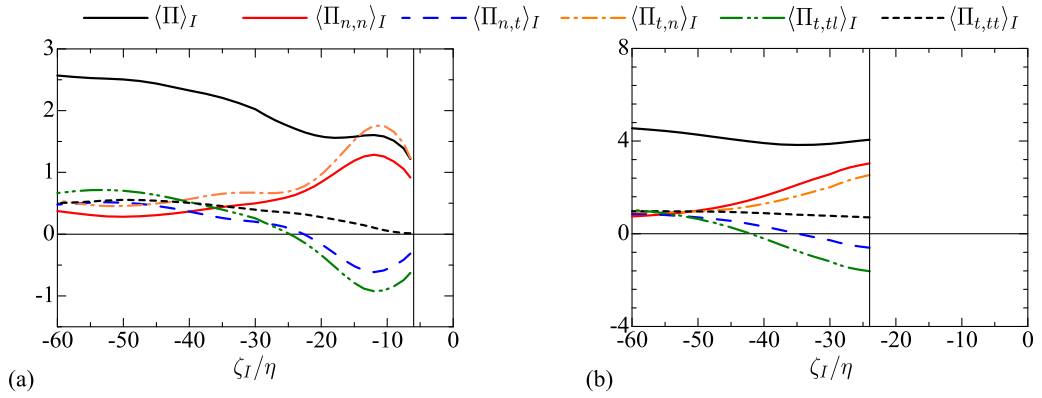

FIG. 11. Conditional averages of decomposed terms of the interscale energy flux, Eqs. (13)–(17), in SFT1: (a) $r/\eta = 6$; (b) $r/\eta = 24$. The results are presented for $|\zeta_I| \geqslant r$.

term are qualitatively similar for $r/\eta = 6$ and 24, and the velocity gradient in the interface normal direction causes the interscale energy transfer to small scales. However, the influence of the TNTI layer appears further away from the interface for the energy flux at larger scales.

Figure 12 complements the information given in the conditional average of the kinetic energy flux Π presented in Fig. 7(c) by showing the probability density function (PDF) of Π for $r/\eta = 4$ at three locations. Even though the mean value of Π is positive, implying a dominating forward energy transfer from large to small scales, both forward and backward transfer events exist. The forward transfer ($\Pi > 0$) becomes less frequent from the TSL toward the VSL as also expected from small $\langle\Pi\rangle_I$ within the VSL.

Figures 13(a)–13(e) show the joint PDF between Π and decomposed terms in Eq. (12) calculated for $(\zeta_I/\eta, r/\eta) = (-10, 10)$. Events with $\Pi > 0$ mostly occur with positive $\Pi_{n,n}$ and $\Pi_{t,n}$ in Figs. 13(a) and 13(c), and the instantaneous energy transfer to small scales is also associated with the velocity gradient in the interface normal direction. In Figs. 13(b) and 13(d), the probability is high for $\Pi > 0$ even for $\Pi_{n,t} < 0$ and $\Pi_{n,tl} < 0$. Thus, although the averages of $\Pi_{n,t}$ and $\Pi_{n,tl}$ are negative, negative $\Pi_{n,t}$ and $\Pi_{n,tl}$ are not directly related to $\Pi < 0$. The comparison of the joint PDF for all decomposed terms indicates that $\Pi < 0$ is not caused by a specific term. Figure 13(f) shows the joint PDF between $\Pi_{n,n}$ and $\Pi_{t,n}$. These terms are positively correlated, and the energy transfer into small scales by $\Pi_{n,n}$ and $\Pi_{t,n}$ often occurs in the same region. Positive $\Pi_{n,n}$ requires $\overline{\partial u_n/\partial\zeta_I} < 0$. As u_n is the velocity in the ζ_I direction, $\overline{\partial u_n/\partial\zeta_I} < 0$ represents a compressive motion

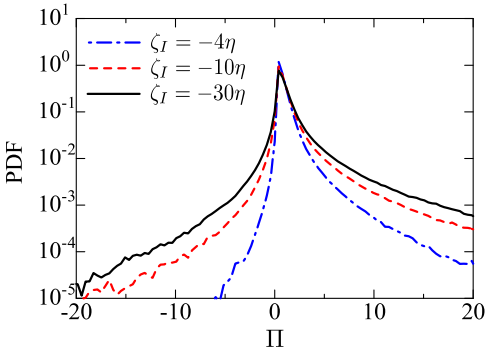

FIG. 12. PDF of the kinetic energy flux Π for $r/\eta = 4$ within the VSL ($\zeta_I/\eta = -4$), TSL ($\zeta_I/\eta = -10$), and turbulent core region ($\zeta_I/\eta = -30$).

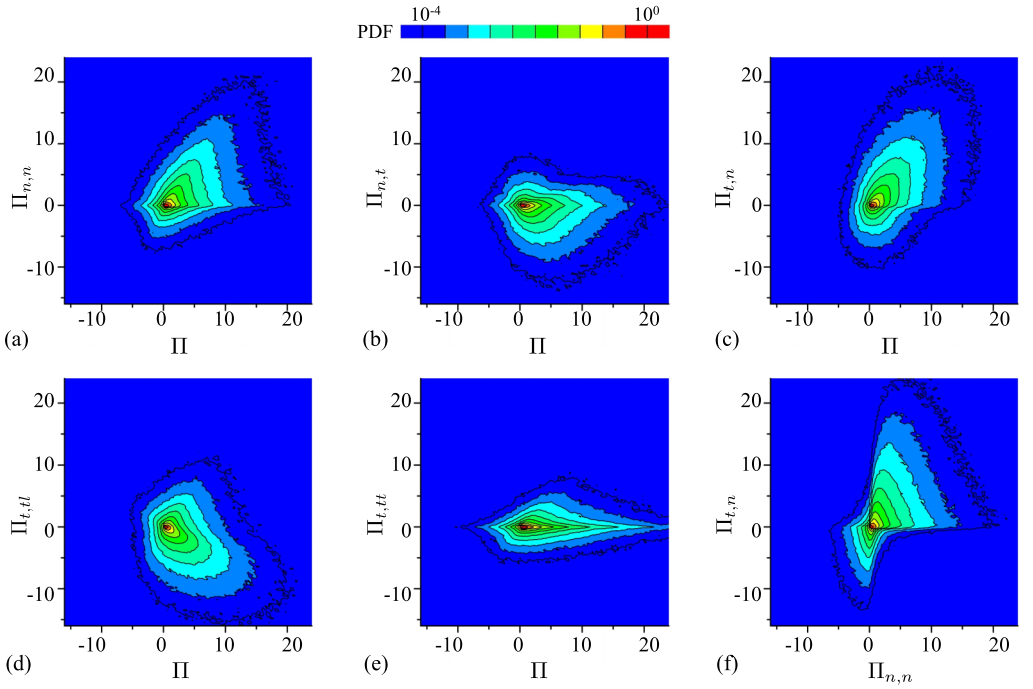

FIG. 13. Joint PDF between Π and decomposed terms in Eqs. (13)–(17): (a) $\Pi_{n,n}$, (b) $\Pi_{n,t}$, (c) $\Pi_{t,n}$, (d) $\Pi_{t,tl}$, (e) $\Pi_{t,tt}$. (f) Joint PDF between $\Pi_{n,n}$ and $\Pi_{t,n}$.

in the interface normal direction. $\Pi_{t,n}$ contain $\overline{\partial u_{t1}/\partial\zeta_I}$ and $\overline{\partial u_{t2}/\partial\zeta_I}$, which can be considered as a shear due to the tangential-velocity jump across the TNTI layer. The compression in the interface normal direction can amplify the tangential-velocity gradients in the interface normal direction, $\overline{\partial u_{t1}/\partial\zeta_I}$ and $\overline{\partial u_{t2}/\partial\zeta_I}$, and therefore $\Pi_{n,n}$ tends be correlated with $\Pi_{n,t}$. Positive $\Pi_{n,n}$ and negative $\Pi_{t,tl}$ near the TNTI layer are consistent with the analysis of the interscale energy transfer based on the Kármán-Howarth-Monin-Hill (KHMH) equation in a turbulent wake [48]. It was shown that stretching motions in the interface tangential direction, related to $\Pi_{t,tl}$ in the present analysis, cause a backward energy transfer, while compressive motions in the interface normal direction, i.e., $\Pi_{n,n}$, cause a forward energy transfer. The analysis of the KHMH equation was conducted on an isosurface used to detect the TNTI layer in the wake. The present analysis conditioned on the distance from the irrotational boundary further confirms that the presence of the interface affects the interscale energy transfer within the entire TNTI layer and even in the turbulent core region when the scale r is large.

V. CONCLUSIONS

The scale dependence of kinetic energy near the TNTI layer was studied with direct numerical simulations of shear-free turbulence. The scale dependence was assessed by using a different diagnostic tool based on the local volume average (low-pass filter) combined with statistics conditioned on the distance from the outer edge of the TNTI layer. The proposed metric is therefore able to decompose the flow into large- and small-scale components, at a fixed distance from the outer edge of the TNTI layer. The local volume average was taken solely with turbulent or nonturbulent regions, and the scale dependence was studied separately for these two regions.

Conditional averages were taken for the small-scale kinetic energy and its transport equation. The presence of the TNTI depletes the kinetic energy at small scales and the interscale energy flux Π into small scales within the VSL. The interscale energy flux was also examined based on the decomposition that considers the velocity vector and its gradient in the interface normal and

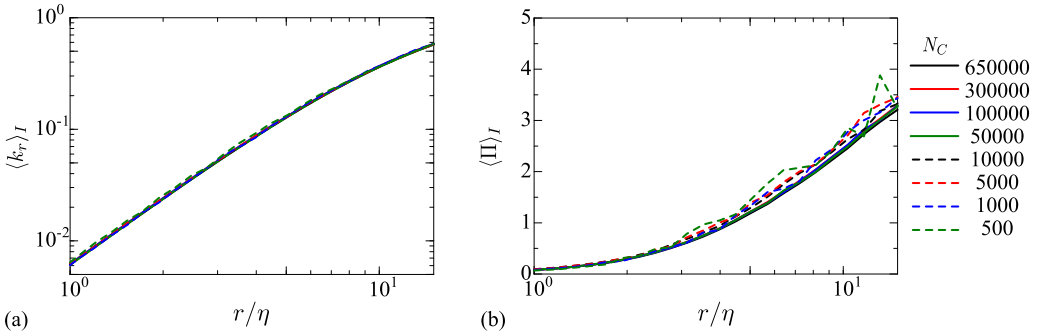

FIG. 14. Dependence of conditional statistics on the different number of samples in SFT1: (a) cumulative kinetic energy; (b) averaged interscale energy flux. These results are obtained at $\zeta_I = -15\eta$ in SFT1.

tangential directions. The present analysis confirmed that the interscale energy transfer from large to small scales is caused by the velocity gradient in the interface normal direction. Here, the energy transfer from large to small scales is caused by fluid compression associated with the gradient of the interface-normal velocity and a shearing motion associated with the gradient of the interface-tangential velocity. The interscale energy transfers by the compression and shear tend to occur in the same region and contribute to the energy flux from large to small scales. The viscous diffusion D_ν is shown to increase the small-scale kinetic energy within the VSL, and this energy growth can be related to the process by which the fluid within the VSL gains enstrophy by viscous diffusion. The turbulent diffusion D_T and diffusion by large- and small-scale interactions D_S are anticorrelated within the TNTI layer. D_S can be expressed in a form that contains the interscale energy flux Π with a negative sign. Although D_T and $-\Pi$ exhibit a negative correlation within the TNTI layer, the correlation is not strong enough to cause a strong correlation between D_T and D_S. The role of the pressure diffusion D_P changes depending on the scale, because it reduces the small-scale kinetic energy within the TSL while increasing the energy at other regions and scales. For scales of about 6η, the pressure diffusion term has a local minimum within the TSL, while the pressure diffusion contributes to an increase of the kinetic energy in the turbulent core region. This profile can be explained by the presence of small-scale vortices within the TSL since the vortex cores often have negative peaks of the pressure diffusion term, which are surrounded by positive values [36]. The results provide the first detailed picture of the kinetic energy dynamics within the TNTI layer as functions of scale and position within the layer, and the proposed approach opens the door to a detailed study of the entrainment mechanism based on the scale dependence of turbulent flows.

ACKNOWLEDGMENTS

This work was partially supported by the "Collaborative Research Project on Computer Science with High-Performance Computing in Nagoya University," and by MEXT KAKENHI Grant Number 16K18013. C.B. da Silva acknowledges Fundação para a ciência e Tecnologia (FCT) through IDMEC, under LAETA Pest-OE/EME/LA0022, and through project PTDC/EMS-ENE/6129/2014.

APPENDIX A: INFLUENCE OF NUMBER OF SAMPLES ON CONDITIONAL STATISTICS

The convergence of conditional statistics depends on the number of points on the irrotational boundary, N_C, for which the statistical samples are taken with the local coordinate ζ_I. Figure 14 shows the cumulative kinetic energy $\langle k_r \rangle_I$ and the averaged interscale energy flux $\langle \Pi \rangle_I$ at $\zeta_I = -15\eta$ obtained for a range of N_C between 5.0×10^2 and 6.5×10^5. $\langle k_r \rangle_I$ is independent of N_C for the range of N_c used here, and one can obtain a well-converged result for $\langle k_r \rangle_I$ even with a small number of

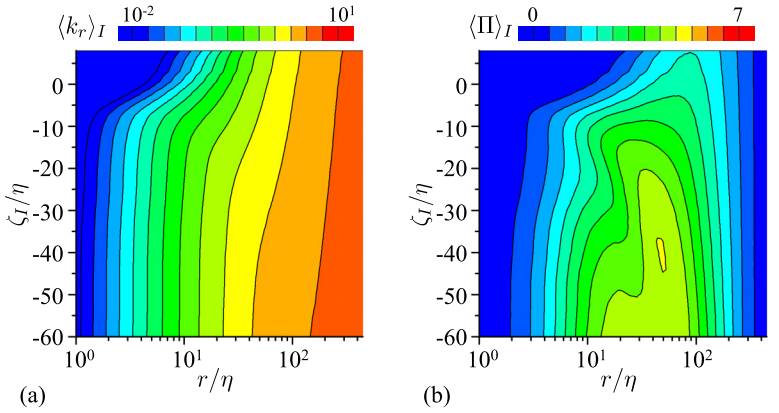

FIG. 15. Conditional statistics calculated with the filter that does not distinguish turbulent and nonturbulent regions: (a) cumulative kinetic energy; (b) averaged interscale energy flux. These results are obtained in SFT1.

samples. On the other hand, $\langle \Pi \rangle_I$ tends to be converged when $N_C > 5.0 \times 10^4$. Here, the points where the local coordinate is defined are almost uniformly distributed on the isosurface of $|\boldsymbol{\omega}| = \omega_{th}$. The order of the distance between two nearby points on the isosurface is estimated as $D = \sqrt{S/N_C}$, where S is the isosurface area of $|\boldsymbol{\omega}| = \omega_{th}$. For $N_C \approx 5.0 \times 10^4$, D/η is about 13 in SFT1, and the local coordinate has to be assigned to the isosurface with spacing smaller than about 13 times the Kolmogorov length scale for the DNS database used in this study.

APPENDIX B: STATISTICS OBTAINED WITH A CONVENTIONAL TOP-HAT LOW-PASS FILTER

The filter used for the scale decomposition is defined with the volume average of either turbulent or nonturbulent regions. This Appendix assesses a filter that does not distinguish between these two regions. This filter is defined by Eq. (1) with G equal to 1 and 0 for $|\boldsymbol{x} - \boldsymbol{x}'| \leqslant r$ and $|\boldsymbol{x} - \boldsymbol{x}'| > r$, respectively. Figure 15 shows the cumulative kinetic energy $\langle k_r \rangle_I$ and interscale energy flux $\langle \Pi \rangle_I$ obtained with this filter. As also found in the profiles obtained with G_T and G_{NT} in Figs. 7(a) and 7(c), $\langle k_r \rangle_I$ and $\langle \Pi \rangle_I$ with small r within the VSL are smaller than in the turbulent core region. However, $\langle k_r \rangle_I$ and $\langle \Pi \rangle_I$ for all length scales decrease from the turbulent toward the nonturbulent region because the nonturbulent region has smaller $\langle k_r \rangle_I$ and $\langle \Pi \rangle_I$ than the turbulent region. Therefore, when the filter is applied without distinguishing the turbulent and nonturbulent regions, it is not clear whether the reduction of $\langle k_r \rangle_I$ and $\langle \Pi \rangle_I$ at small r within the TNTI layer is related to the properties of the TNTI layer or the influence of the nonturbulent region mixed in the statistics calculated in the turbulent region. Here, the present results do not suggest that a low-pass filter used in the study of TNTI layers should always distinguish turbulent and nonturbulent regions. For example, when the performance of subgrid-scale models is assessed near the TNTI layer, a low-pass filter that defines grid and subgrid scales should be applied without distinguishing the two regions because computational grids in large-eddy simulations are usually too coarse to resolve thin TNTI layers [49–51].

[1] C. B. da Silva, J. C. R. Hunt, I. Eames, and J. Westerweel, Interfacial layers between regions of different turbulence intensity, Annu. Rev. Fluid Mech. **46**, 567 (2014).

[2] M. Holzner and B. Lüthi, Laminar Superlayer at the Turbulence Boundary, Phys. Rev. Lett. **106**, 134503 (2011).

[3] D. K. Bisset, J. C. R. Hunt, and M. M. Rogers, The turbulent/non-turbulent interface bounding a far wake, J. Fluid Mech. **451**, 383 (2002).
[4] J. Westerweel, C. Fukushima, J. M. Pedersen, and J. C. R. Hunt, Mechanics of the Turbulent-Nonturbulent Interface of a Jet, Phys. Rev. Lett. **95**, 174501 (2005).
[5] A. Attili, J. C. Cristancho, and F. Bisetti, Statistics of the turbulent/non-turbulent interface in a spatially developing mixing layer, J. Turbul. **15**, 555 (2014).
[6] T. Watanabe, Y. Sakai, K. Nagata, Y. Ito, and T. Hayase, Enstrophy and passive scalar transport near the turbulent/non-turbulent interface in a turbulent planar jet flow, Phys. Fluids **26**, 105103 (2014).
[7] M. van Reeuwijk and M. Holzner, The turbulence boundary of a temporal jet, J. Fluid Mech. **739**, 254 (2014).
[8] N. S. Vaghefi and C. K. Madnia, Local flow topology and velocity gradient invariants in compressible turbulent mixing layer, J. Fluid Mech. **774**, 67 (2015).
[9] R. Jahanbakhshi and C. K. Madnia, Viscous superlayer in a reacting compressible turbulent mixing layer, J. Fluid Mech. **848**, 743 (2018).
[10] G. Balamurugan, A. Rodda, J. Philip, and A. C. Mandal, Characteristics of the turbulent non-turbulent interface in a spatially evolving turbulent mixing layer, J. Fluid Mech. **894**, A4 (2020).
[11] K. Chauhan, J. Philip, C. M. de Silva, N. Hutchins, and I. Marusic, The turbulent/non-turbulent interface and entrainment in a boundary layer, J. Fluid Mech. **742**, 119 (2014).
[12] J. Eisma, J. Westerweel, G. Ooms, and G. E. Elsinga, Interfaces and internal layers in a turbulent boundary layer, Phys. Fluids **27**, 055103 (2015).
[13] T. Ishihara, H. Ogasawara, and J. C. R. Hunt, Analysis of conditional statistics obtained near the turbulent/non-turbulent interface of turbulent boundary layers, J. Fluids Struct. **53**, 50 (2015).
[14] G. Borrell and J. Jiménez, Properties of the turbulent/non-turbulent interface in boundary layers, J. Fluid Mech. **801**, 554 (2016).
[15] J. Lee, H. J. Sung, and T. A. Zaki, Signature of large-scale motions on turbulent/non-turbulent interface in boundary layers, J. Fluid Mech. **819**, 165 (2017).
[16] K. N. Helland, C. W. Van Atta, and G. R. Stegen, Spectral energy transfer in high Reynolds number turbulence, J. Fluid Mech. **79**, 337 (1977).
[17] J. A. Domaradzki, W. Liu, C. Härtel, and L. Kleiser, Energy transfer in numerically simulated wall-bounded turbulent flows, Phys. Fluids **6**, 1583 (1994).
[18] R. J. Hill, Exact second-order structure-function relationships, J. Fluid Mech. **468**, 317 (2002).
[19] N. Marati, C. M. Casciola, and R. Piva, Energy cascade and spatial fluxes in wall turbulence, J. Fluid Mech. **521**, 191 (2004).
[20] L. Danaila, J. F. Krawczynski, F. Thiesset, and B. Renou, Yaglom-like equation in axisymmetric anisotropic turbulence, Phys. D (Amsterdam, Neth.) **241**, 216 (2012).
[21] P. C. Valente and J. C. Vassilicos, The energy cascade in grid-generated non-equilibrium decaying turbulence, Phys. Fluids **27**, 045103 (2015).
[22] A. Cimarelli, G. Cocconi, B. Frohnapfel, and E. De Angelis, Spectral enstrophy budget in a shear-less flow with turbulent/non-turbulent interface, Phys. Fluids **27**, 125106 (2015).
[23] T. Watanabe, C. B. da Silva, and K. Nagata, Non-dimensional energy dissipation rate near the turbulent/non-turbulent interfacial layer in free shear flows and shear free turbulence, J. Fluid Mech. **875**, 321 (2019).
[24] G. L. Eyink, Locality of turbulent cascades, Phys. D (Amsterdam, Neth.) **207**, 91 (2005).
[25] H. Aluie, Compressible Turbulence: The Cascade and its Locality, Phys. Rev. Lett. **106**, 174502 (2011).
[26] J. Wang, Y. Yang, Y. Shi, Z. Xiao, X. T. He, and S. Chen, Cascade of Kinetic Energy in Three-Dimensional Compressible Turbulence, Phys. Rev. Lett. **110**, 214505 (2013).
[27] O. Terashima, Y. Sakai, K. Nagata, Y. Ito, K. Onishi, and Y. Shouji, Simultaneous measurement of velocity and pressure near the turbulent/non-turbulent interface of a planar turbulent jet, Exp. Therm. Fluid Sci. **75**, 137 (2016).
[28] C. B. da Silva, The behavior of subgrid-scale models near the turbulent/nonturbulent interface in jets, Phys. Fluids **21**, 081702 (2009).

[29] T. S. Silva, M. Zecchetto, and C. B. da Silva, The scaling of the turbulent/non-turbulent interface at high Reynolds numbers, J. Fluid Mech. **843**, 156 (2018).
[30] T. Watanabe, Y. Sakai, K. Nagata, Y. Ito, and T. Hayase, Turbulent mixing of passive scalar near turbulent and non-turbulent interface in mixing layers, Phys. Fluids **27**, 085109 (2015).
[31] R. R. Taveira, J. S. Diogo, D. C. Lopes, and C. B. da Silva, Lagrangian statistics across the turbulent-nonturbulent interface in a turbulent plane jet, Phys. Rev. E **88**, 043001 (2013).
[32] R. Jahanbakhshi, N. S. Vaghefi, and C. K. Madnia, Baroclinic vorticity generation near the turbulent/non-turbulent interface in a compressible shear layer, Phys. Fluids **27**, 105105 (2015).
[33] T. Watanabe, Y. Sakai, K. Nagata, Y. Ito, and T. Hayase, Vortex stretching and compression near the turbulent/nonturbulent interface in a planar jet, J. Fluid Mech. **758**, 754 (2014).
[34] T. Watanabe, X. Zhang, and K. Nagata, Turbulent/non-turbulent interfaces detected in DNS of incompressible turbulent boundary layers, Phys. Fluids **30**, 035102 (2018).
[35] U. Piomelli, Y. Yu, and R. J. Adrian, Subgrid-scale energy transfer and near-wall turbulence structure, Phys. Fluids **8**, 215 (1996).
[36] C. B. da Silva and O. Métais, On the influence of coherent structures upon interscale interactions in turbulent plane jets, J. Fluid Mech.**473**, 103 (2002).
[37] R. R. Taveira and C. B. da Silva, Characteristics of the viscous superlayer in shear free turbulence and in planar turbulent jets, Phys. Fluids **26**, 021702 (2014).
[38] K. Takamure, Y. Ito, Y. Sakai, K. Iwano, and T. Hayase, Momentum transport process in the quasi self-similar region of free shear mixing layer, Phys. Fluids **30**, 015109 (2018).
[39] T. Watanabe, Y. Sakai, K. Nagata, Y. Ito, and T. Hayase, Wavelet analysis of coherent vorticity near the turbulent/non-turbulent interface in a turbulent planar jet, Phys. Fluids **26**, 095105 (2014).
[40] S. B. Pope, *Turbulent Flows* (Cambridge University Press, Cambridge, UK, 2000).
[41] C. B. da Silva, R. J. N. Dos Reis, and J. C. F. Pereira, The intense vorticity structures near the turbulent/non-turbulent interface in a jet, J. Fluid Mech. **685**, 165 (2011).
[42] O. M. Phillips, The irrotational motion outside a free turbulent boundary, in *Proceedings of the Cambridge Philosophical Society* (Cambridge University Press, Cambridge, UK, 1955), Vol. 51, pp. 220–229.
[43] D. J. Carruthers and J. C. R. Hunt, Velocity fluctuations near an interface between a turbulent region and a stably stratified layer, J. Fluid Mech.**165**, 475 (1986).
[44] C. B. da Silva and J. C. F. Pereira, Invariants of the velocity-gradient, rate-of-strain, and rate-of-rotation tensors across the turbulent/nonturbulent interface in jets, Phys. Fluids **20**, 055101 (2008).
[45] M. Holzner, A. Liberzon, N. Nikitin, B. Lüthi, W. Kinzelbach, and A. Tsinober, A Lagrangian investigation of the small-scale features of turbulent entrainment through particle tracking and direct numerical simulation, J. Fluid Mech. **598**, 465 (2008).
[46] F. A. Portela, G. Papadakis, and J. C. Vassilicos, The turbulence cascade in the near wake of a square prism, J. Fluid Mech. **825**, 315 (2017).
[47] T. Watanabe, C. B. da Silva, K. Nagata, and Y. Sakai, Geometrical aspects of turbulent/non-turbulent interfaces with and without mean shear, Phys. Fluids **29**, 085105 (2017).
[48] Y. Zhou and J. C. Vassilicos, Energy cascade at the turbulent/nonturbulent interface, Phys. Rev. Fluids **5**, 064604 (2020).
[49] M. Gampert, K. Kleinheinz, N. Peters, and H. Pitsch, Experimental and numerical study of the scalar turbulent/non-turbulent interface layer in a jet flow, Flow, Turbul. Combust. **92**, 429 (2014).
[50] C. B. da Silva, D. C. Lopes, and V. Raman, The effect of subgrid-scale models on the entrainment of a passive scalar in a turbulent planar jet, J. Turbul. **16**, 342 (2015).
[51] T. Watanabe, Y. Sakai, K. Nagata, and Y. Ito, Large eddy simulation study of turbulent kinetic energy and scalar variance budgets and turbulent/non-turbulent interface in planar jets, Fluid Dyn. Res. **48**, 021407 (2016).